CHEMISTRY OF MATERIALS

Article

pubs.acs.org/cm

Additive-Driven Self-Assembly of Well-Ordered Mesoporous Carbon/Iron Oxide Nanoparticle Composites for Supercapacitors

Ying Lin, Xinyu Wang, Gang Qian, and James J. Watkins*

Department of Polymer Science and Engineering, University of Massachusetts Amherst, 120 Governors Drive, Amherst, Massachusetts 01003, United States

Supporting Information

ABSTRACT: Ordered mesoporous carbon/iron oxide composites were prepared by cooperative self-assembly of poly(*t*-butyl acrylate)-block-polyacrylonitrile (PtBA-*b*-PAN), which contains both a carbon precursor block and a porogen block, and phenol-functionalized iron oxide nanoparticles (NPs). Because of the selective hydrogen bonding between the phenol-functionalized iron oxide NPs and PAN, the NPs were preferentially dispersed in the PAN domain and subsequently within the mesoporous carbon framework. Ordered mesoporous carbon nanocomposites with Fe_2O_3 NPs mass loadings as high as 30 wt % were obtained upon carbonization at the block copolymer composites at 700 °C. The morphology of the mesoporous composites was studied using small-angle X-ray scattering (SAXS), transmission electron microscopy (TEM), and N_2 adsorption. The results confirmed high-fidelity preservation of morphology of the NP-doped block copolymer composites in the mesoporous carbon composites. The electrochemical performance of the mesoporous composite films improved significantly upon the addition of iron oxide NPs. The specific capacitance (C_g) of neat mesopororous carbon films prepared from PtBA-*b*-PAN was 153 F/g at a current density of 0.5 A/g, whereas films containing 16 and 30 wt % Fe_2O_3 present as well-dispersed NPs within the mesoporous carbon framework exhibited capacitances of 204 and 235 F/g, respectively. The well-defined mesoporous in the template carbon structure together with high loadings of iron oxide nanoparticles are promising for use in supercapacitor applications.

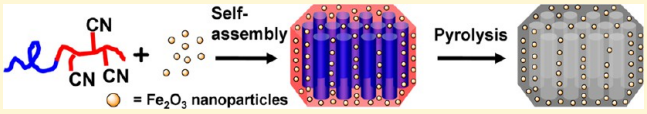

INTRODUCTION

Supercapacitors have attracted significant attention as energy-storage devices for applications such as starting automotives and the regenerating of brake energy to meet the requirements of fast charge and discharge, high power density, and long cycle life.[1] According to their mechanism of energy storage, supercapacitors are classified as either electric double-layer capacitors (EDLC)[2] or faradaic pseudocapacitors. EDLCs use carbon-based materials such as activated carbon,[3] mesoporous carbon,[4] graphene,[5] or carbon nanotubes.[6,7] Because of the fast sorption and desorption of ions, carbon-based supercapacitors usually have high power capabilities and good conductivity but a low specific energy, as only the surface of the carbon is accessed.[8,9] Pseudocapacitors, however, exploit the pseudocapacitance behavior of redox-active materials such as transition-metal oxides[10−14] or conductive polymers[15−18] and typically have high energy density, as the bulk of the material, not just the surface layer, is utilized. However, one significant drawback of these materials is the relatively low power density because of slow diffusion of ions within the bulk of the electrode. These trade-offs have inspired attempts to develop hybrid supercapacitors by combining carbon-based materials with redox-active materials.

Among the hybrid approaches, metal-oxide/mesoporous carbon combinations have shown great potential.[19] Because of their high surface area, electrical conductivity, uniform pore size, and well-defined channel structures, mesoporous carbons are the most frequently used materials as supports for metal oxides.[4,20] To improve performance, it is often necessary to incorporate metal-oxide particles within the nanostructured carbon supports. Although metal oxides possess high pseudocapacitance values, their real contribution to the total charge storage depends strongly on the surface utilization of the active materials, which could be achieved by dispersing nanosized particles onto highly ordered high-surface-carbon substrates. Thus far, many different metal-oxides nanoparticles have been reported to be incorporated into mesoporous carbons using various methods, including direct deposition,[21,22] ion exchange,[23,24] diffusion followed by oxidation,[25] in situ reduction,[26] and sonochemical approaches.[27] Whereas some of the methods are time-consuming and tedious, among these, a one-pot triconstituent coassembly approach[28,29] in which the carbon precursors and inorganic precursors are assembled within a structure-directing block copolymer is potentially facile and cost-effective. Zhao[30] and Wang[31] et al. realized the synthesis of highly ordered Fe-containing mesoporous carbon materials using phenolic resol as a carbon source, ferric citrate[30] or iron nitrite[31] as an iron source, and an amphiphilic poly(ethylene oxide-*b*-propylene oxide-*b*-ethyleneoxide) triblock copolymer, Pluronic F127, as the template. However, in situ preparation of the Fe_2O_3 nanoparticles resulted in NPs that were significantly larger than the pore walls and extended

Received: December 23, 2013
Revised: February 21, 2014
Published: February 21, 2014

Scheme 1. Schematic of the Preparation of Mesoporous Carbon/Iron Oxide Nanocomposites Using Additive-Driven Self-Assembly

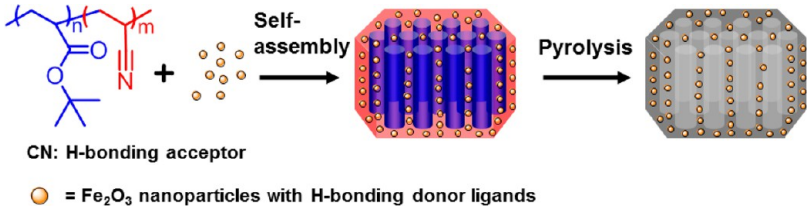

from the carbon walls into mesopore channels, especially at high loadings, increasing the roughness of the pore surface and compromising the regular mesoscopic structure. This results in both decreased surface utilization of the active materials and increased tortuosity for ion transport. Metal salts have also been utilized to form nanoparticles within carbon aerogels,[32] but these salts can interfere with self-assembly of the surfactant template and often lead to disordered carbon frameworks or reduced porosity. More recently, the Vogt group synthesized mesoporous carbon composite thin films containing cobalt and vanadium oxides by triconstituent self-assembly of cobalt (or vanadyl) acetylacetonate (acac) as the metal source.[20] Their results showed that even after 500 cycles the composite films maintain a specific capacitance as high as 113 (for Co) and 159 F/g (for V) in comparison to the neat carbon, which exhibited approximately 22 F/g. Collectively, these recent results demonstrate that the metal-oxide−carbon nanocomposite materials are indeed a class of promising electrode materials for high-performance supercapacitors. However, several major drawbacks for metal-oxide−carbon nanocomposite materials remain, such as relatively low loadings of the metal oxide, aggregation of nanoparticles, and the lack of an ordered mesoporous structure.

Herein, we report a straightforward preparation of mesoporous carbon/iron oxide nanoparticle composites via biconstituent cooperative self-assembly of poly(*t*-butyl acrylate)-block-polyacrylonitrile (PtBA-*b*-PAN) and Fe_2O_3 nanoparticles followed by a direct carbonization (Scheme 1). More specifically, we synthesized diblock copolymers composed of polyacrylonitrile, a carbon precursor, and a nanostructure template, and we blended them with Fe_2O_3 nanoparticles decorated with ligands containing phenols. Hydrogen-bond interactions between the phenol ligands on the Fe_2O_3 nanoparticles and polyacrylonitrile accomplishes a number of important goals for well-defined mesoporous composites. These include providing control of the nanoparticle distribution, avoidance of the aggregation of the nanoparticles at high loadings by limiting physical mobility of the nanoparticles, and retaining/enhancing the phase segregation of block copolymer. This approach builds on our recent reports of the use of segment-specific hydrogen-bond interactions between functionalized nanoparticles and block copolymers to prepare well-ordered hybrid materials at high additive loadings.[33−35] Herein, the utilization of hydrogen bonding provides a new way to form carbon−metal-oxide domains within a block copolymer self-assembled nanostructure. In this article, we emphasize the morphology of the composites and the loading of the nanoparticles as well as their utility for obtaining desirable device properties.

EXPERIMENTAL SECTION

Materials. Acrylonitrile (AN), *t*-butyl acrylate (tBA), isobutyryl bromide, *N*,*N*,*N*′,*N*″,*N*″-pentamethyldiethylenetriamine (PMDETA), 2,2′-bipyridyl (bpy), CuBr, CuI, iron(II) acetylacetonate, trioctylphosphine, sodium sulfite, anisole, dimethylformamide (DMF), tetrahydrofuran (THF), ethanol, and methanol were purchased from Sigma-Aldrich. 4-Hydroxybenzoic acid and oleylamine were purchased from Acros Organics. CuI and CuBr were purified by stirring in glacial acetic acid followed by washing with ether and drying overnight under vacuum. Monomers were passed through a basic alumina column prior to use. All other reagents were used as received unless otherwise stated.

Synthesis of PtBA-*b*-PAN Block Copolymers. Poly(*t*-butyl acrylate)-block-polyacrylonitrile (PtBA-*b*-PAN) was synthesized by atom-transfer radical polymerization (ATRP) according to a modified literature procedure.[36] A typical synthesis procedure was as follows. First, PtBA macroinitiator was prepared: 0.16 g of PMDETA (9.5×10^{-4} mol) was dissolved in 20 mL of tBA (17.88 g, 1.40×10^{-1} mol) and 20 mL of anisole in a Schlenk flask. The mixture was then degassed by three freeze−pump−thaw cycles, the flask was filled with nitrogen, and 0.13 g of CuBr (9.5×10^{-4} mol) was added while the mixture was still frozen. Then, the flask was sealed, and air was removed by evacuating the flask and backfilling with nitrogen several times. After thawing the mixture, the reaction flask was immersed in oil-bath heated at 70 °C, and the initiator isobutyryl bromide (0.14g, 9.5×10^{-4} mol) was added through the side arm. After 10 h, the reaction was terminated by the addition of aerated THF and passed through a column filled with alumina to remove the catalyst. Then, the solvent was removed by evaporation, and the PtBA was dried under vacuum at 60 °C to constant weight. The molecular weight based on PS standards was equal to $M_n = 1.44 \times 10^4$ g/mol, and $M_w/M_n = 1.16$.

PtBA-*b*-PAN copolymers were prepared using the macroinitiators: 2.0 g of the above PtBA macroinitiator (1.39×10^{-4} mol), 5 mL of AN (4.03g, 7.60×10^{-2} mol), and 5 mL of DMF were mixed in a Schlenk flask. The flask was subjected to three freeze−pump−thaw cycles. Then, 2.89×10^{-2} g of CuI (1.52×10^{-4} mol) and 4.76×10^{-2} g of bpy (3.04×10^{-4} mol) were added to the flask as above and purged by backfilling with nitrogen. The reaction was carried out at 70 °C for 20 h. The polymer was precipitated by adding the DMF solution to a large excess of methanol. The molecular weight of the copolymer based on PS standards was $M_n = 3.77 \times 10^4$ g/mol, and $M_w/M_n = 1.26$.

Hydrophobic Iron Oxide Nanoparticle Synthesis. The synthesis of iron oxide (Fe_2O_3) nanoparticles was modified on the basis of Park's method for Ni and NiO nanoparticles.[37] Iron(II) acetylacetonate (0.26 g, 1 mmol), oleylamine (1 mL), and trioctylphosphine (5 mL) were mixed in a 25 mL three-necked round-bottomed flask. Residue oxygen was removed by freeze−pump−thaw for three times, and the flask was protected with N_2. The reaction was heated at 100 °C and equilibrated for 10 min to ensure that the reagents were evenly mixed. It was then ramped to 200 °C and cured for 30 min. The resulting nanoparticles were collected by centrifugation with ethanol as the antisolvent. Particles were usually washed with hexanes and ethanol another two to three times to remove excessive ligands.

Hydrophilic Nanoparticle Synthesis. In a typical ligand-exchange reaction,[38] 50 mg of the hydrophobic nanoparticle powder and 500 mg of 4-hydroxylbenzoic acid were mixed with 20 mL of solvent (ethanol, methanol, tetrahydrofuran, or *N*,*N*-dimethylforma-

dx.doi.org/10.1021/cm404199z | *Chem. Mater.* 2014, 26, 2128−2137

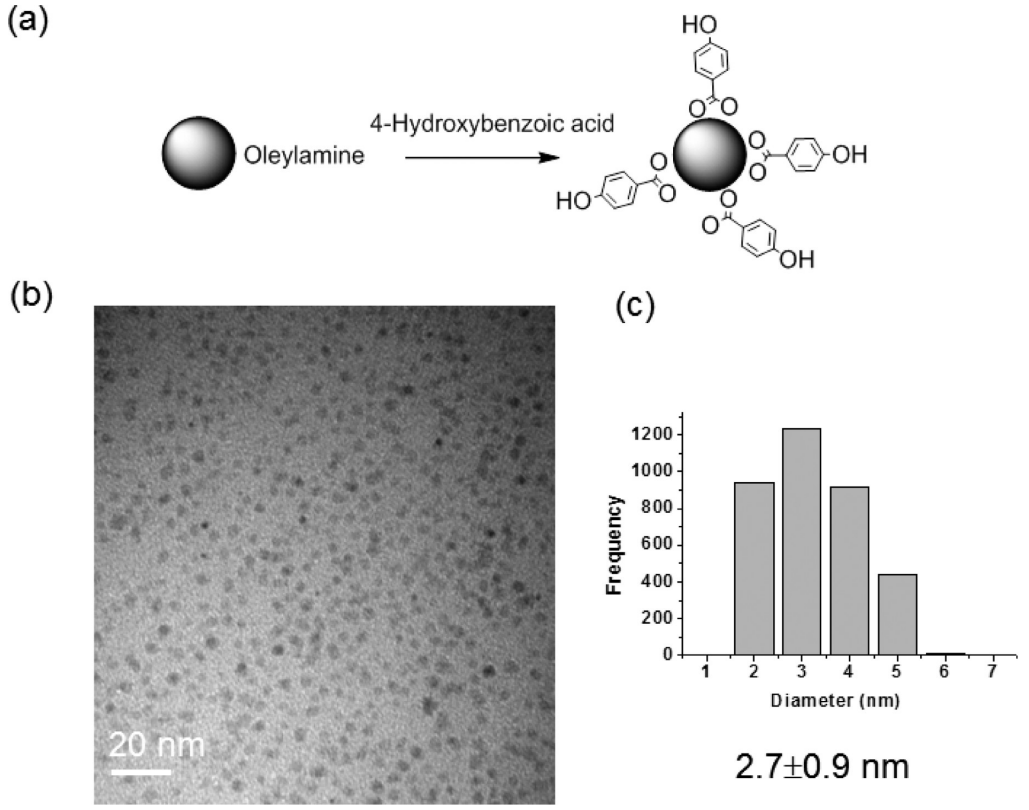

Figure 1. (a) Schematic illustration of the ligand-exchange process, (b) TEM images of Fe_2O_3-OH NPs, and (c) histogram of Fe_2O_3-OH NPs size distribution showing that the average size is 2.7 ± 0.9 nm.

mide) in a scintillation vial. The vial was sonicated for 10 min followed by magnetic stirring for 1 h to ensure that the reaction was complete. Within 5 min, the contents of the reaction vial became a dark yet transparent solution, indicating the dispersion of nanoparticles in the polar solvents. The exchanged nanoparticles were precipitated by the addition of excessive hexanes as the antisolvent and collected by centrifugation. The resulting nanoparticles were then redispersed in ethanol, precipitated by excessive hexanes, and collected by centrifugation. The purification procedures were applied as necessary until all of the excessive ligands were removed. The purified nanoparticles could be easily dispersed in polar organic solvents such as ethanol, methanol, 2-propanol, tetrahydrofuran, or *N*,*N*-dimethylformamide and remain quite stable during the period of observation (over a year).

Preparation of Mesoporous Carbon/Iron Oxide Composites. For preparing block copolymer/iron oxide nanocomposites, appropriate amounts of the block copolymer and dried nanoparticle powder were weighed and dissolved in DMF to form 10% (w/v) stock solutions. The solution was stirred for 1 day and then cast on a glass slide and dried at room temperature, allowing the solvent to slowly evaporate over 24 h. The blend was then annealed at 120 °C under vacuum for 36 h and slowly cooled to room temperature. For preparing mesoporous carbon/iron oxide nanocomposites, the above-mentioned block copolymer/iron oxide nanocomposites were stabilized by cyclization of the nitrile side groups at 280 °C for 2 h under air flow (100 mL/min) with a heating rate of 20 °C/min, purged with nitrogen gas for 1 h during cooling, and then carbonized at 700 °C for 0.5 h under a nitrogen gas flow (100 mL/min) with a heating rate of 10 °C/min.

Characterization. Molecular weights of the polymers were estimated by gel-permeation chromatography (GPC) using DMF as the eluent against polystyrene standards with a refractive index detector. The mass change during the carbonization was monitored by thermogravimetric analysis (TGA). TGA experiments were performed on a TGA2950 thermogravimetric analyzer with a heating rate of 10 °C/min under a N_2 atmosphere. Infrared spectroscopic measurements were performed using a Bruker Vertex 70 FTIR spectrophotometer in ATR mode.

Small-angle X-ray scattering (SAXS) was performed using an Rigaku-Molecular Metrology SAXS equipment using 0.1542 nm (Cu Kα radiation) and an incident beam of 0.4 mm in diameter. The sample-to-detector distance was calibrated using a silver behenate standard peak at 1.076 nm^{-1}. X-ray photoelectron spectroscopy (XPS) data was performed using a Physical Electronics Quantum 2000 at two takeoff angles, 15 and 75°, between the plane of the sample surface and the entrance lens of the detector optics. N_2 adsorption and desorption experiments were performed on an Autosorb-1 system at 77 K. The specific surface area was determined by using the Brunauer–Emmett–Teller (BET) method. The micropore volume was determined by using conventional t-plot methods from adsorption data over t ranges from 3 to 5 Å. Transmission electron microscopy (TEM) was performed on films using a JEOL 2000 FX microscope operating at 200 kV. Thin sections for microscopy were prepared using a Leica Ultracut UCT microtome equipped with a Leica EM FCS cryogenic sample chamber operated at room temperature. Sections were approximately 50 nm in thickness. Samples after carbonization were scraped from the silicon substrate, crushed with a mortar and pestle, diluted with ethanol, and then deposited on a carbon-coated copper TEM grid.

Electrochemical measurements were carried out in a three-electrode cell with a Pt wire counter electrode and Ag/AgCl reference electrode using a CHI660E electrochemical analyzer (CH Instruments Inc.). Stainless steel was used as the film substrate to serve as the current collector for working electrode application. Electrochemical tests were conducted in 1 M Na_2SO_3 at ambient temperature with aqueous potentials referenced against Ag/AgCl. The cyclic voltammetry (CV) curves were obtained at various scan rates from 1 to 100 mV/s in the range of −1.0 to −0.2 V. Galvanostatic charge–discharge (GCD) curves were obtained at various current densities from 0.5 to 10 A/g in

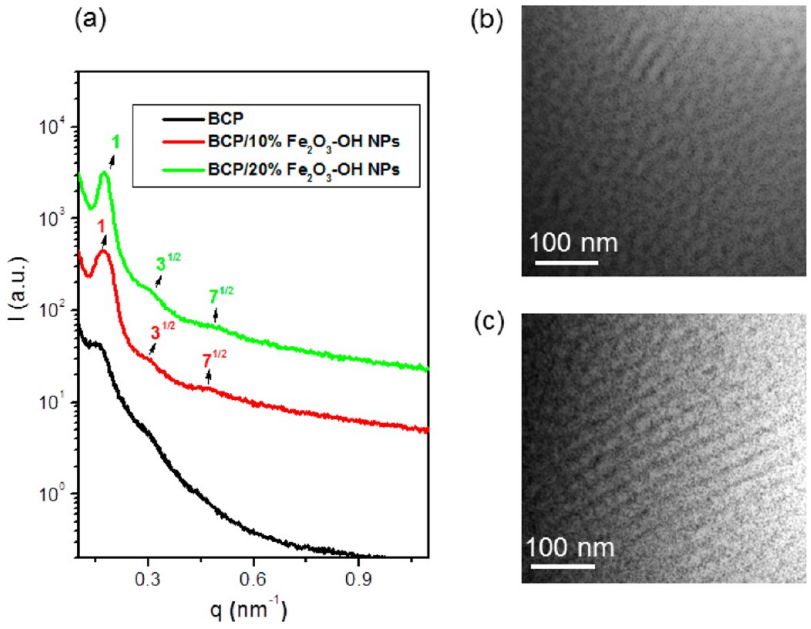

Figure 2. (a) Overlay of SAXS profiles of the PtBA-*b*-PAN block copolymer and its blends with Fe_2O_3-OH nanoparticles before carbonization. TEM images of the blend of the BCP with (b) 10 wt % Fe_2O_3-OH NPs and (c) 20 wt % Fe_2O_3-OH NPs before carbonization. All of the samples are annealed at 150 °C for 2 days.

the range of −1.0 to 0.1 V. Cycling test was conducted on a Maccor model 4304 battery and cell test equipment.

RESULTS AND DISCUSSION

Synthesis and Characterization of PtBA-*b*-PAN Block Copolymer and Fe_2O_3 Nanoparticles. It has been well-documented that PAN can be used for the manufacture of carbon fibers (black Orlon) by the process of thermal stabilization. When PAN is heated, it decomposes by cyclization and aromatization of the nitrile side groups, with some intermolecular cross-linking, to yield carbon fibers.[39] This cyclization is of interest because it can be used to freeze in a specific microstructure, which, in the present case, is that of a microphase-separated diblock copolymer. Further pyrolysis can then be performed to create nanostructured carbon materials. The creation of carbon arrays by employing this method has been demonstrated by Kowalewski et al. using poly(acrylonitrile-*b*-*n*-butyl acrylate-*b*-acrylonitrile),[36] by Russell et al. using poly(styrene-*b*-acrylonitrile),[40] and by others. The approach described herein employs microphase-separated PtBA-*b*-PAN diblock copolymers as nanoporous carbon templates. The PtBA-*b*-PAN block copolymer was synthesized following the procedure of Matyjaszewski and co-workers[36] using an atom-transfer radical polymerization (ATRP) method (see Figure S1). This method assures a high level of control over the block length and composition in order to maintain control of the nanoscale morphology arising from phase separation of the blocks. Several block and gradient copolymers were prepared, but throughout this study, we focused on the diblock copolymer of *t*-butyl acrylate (tBA) and acrylonitrile (AN) with average composition PtBA (14.4K)-*b*-PAN (23.3K) and polydispersity M_w/M_n = 1.26, where M_w and M_n are the weight and number average molecular weights, respectively.

Iron oxide nanoparticles were prepared according to a slight modification of literature methods.[37] The as-synthesized nanoparticles are passivated with oleylamine ligands wherein the amine groups adsorb to the metal-oxide core. Preformed Fe_2O_3 nanoparticles rather than the metal-oxide precursors were employed in our strategy to ensure high surface area and because in situ reduction reactions to form metal oxides will affect both the assembly process and the final composite morphology. To enable H-bonding with the polymer, the surface of the iron oxide nanoparticles was modified by employing ligand exchange[38] to replace the long alkyl chain ligands with a more effective interfacial molecule. 4-Hydroxylbenzoic acid was chosen as the target ligand based on the following two characteristics. First, the acid group has strong binding affinity with iron oxide core. Second, the remaining phenolic OH group acts as a H-bonding donor and interacts strongly with the nitrile group in the PAN block.[41] The iron oxide nanoparticles were 2.7 ± 0.9 nm in diameter, smaller than the size of nanoparticles that are usually realized using in situ preparation.[29] A representative TEM image of the NPs is shown in Figure 1. Thermal gravimetric analysis (TGA) indicates that the iron oxide core composes ∼59.3% of the mass of the phenol-functionalized iron oxide nanoparticles (Fe_2O_3-OH NPs). To investigate the stability of the ligands during the stabilization of the PAN, TGA was conducted on the nanoparticles under the same conditions as those for the PAN stabilization. After heating the functionalized NPs in air at 20 °C/min to 280 °C and holding at this temperature and atmosphere for 2 h, the weight loss of NPs was about 24.0%. Therefore, at least 16% of ligands or ligand-decomposition products remain during PAN stabilization.

We employed FTIR to verify the interaction between Fe_2O_3-OH NPs and the PAN chain segments because of this method's sensitivity to hydrogen-bond formation. Figure S2 shows infrared spectra for PtBA-*b*-PAN, Fe_2O_3-OH NPs, and their blends. The monomodal peak centered at 2243 cm^{-1} is characteristic of the symmetric stretching mode of the C≡N groups. Because the C≡N is adjacent to tertiary C, it shows weak intensity. When PtBA-*b*-PAN is blended with Fe_2O_3-OH NPs, the monomodal peak from the C≡N is clearly split into two bands centered at 2243 and 2262 cm^{-1}. The shoulder in

dx.doi.org/10.1021/cm404199z | *Chem. Mater.* 2014, 26, 2128−2137

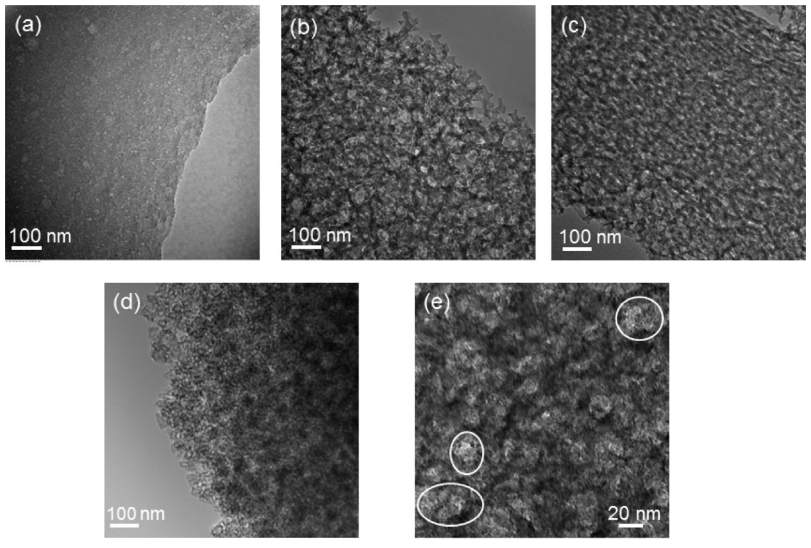

Figure 3. TEM images of various PAN-based materials after carbonization (a) PAN homopolymer, (b) PtBA-*b*-PAN BCP, (c) BCP/10% Fe_2O_3-OH NPs, and (d, e) BCP/20% Fe_2O_3-OH NPs, the highlighted circles in panel e shows that the individual nanoparticles remain intact after carbonization.

the vicinity of 2262 cm^{-1} is attributable to the C≡N bonded to phenol, indicating the nitrile−hydroxyl interaction is present.[42]

Morphology Characterization of Block Copolymer/ Fe_2O_3-OH Nanoparticles Blends. Figure 2a shows small-angle X-ray scattering (SAXS) profiles for PtBA-*b*-PAN and blends of this BCP with Fe_2O_3-OH NPs at several NP concentrations. The concentrations of the NPs are expressed as the weight percent of the entire composite based on the mass of the NP cores and ligand shells. The SAXS curves were shifted vertically for clarity. The neat PtBA-*b*-PAN exhibited a broad hump, which is due to the correlation hole effect observed for disordered BCPs,[43,44] pointing to the absence of well-defined nanoscale morphology. This is similar as the reported SAXS profile of poly(*n*-butyl acrylate-*b*-acrylonitrile) in the literature.[45] Upon addition of 10 wt % Fe_2O_3-OH NPs, multiple scattering peaks were observed at 0.171, 0.296, and 0.452 nm^{-1} (peak position ratios relative to q^* of 1, $3^{1/2}$, $7^{1/2}$, ... with a *d*-spacing of 36.7 nm ($d_{100} = 2\pi/q^*$)). These higher-order reflections result from structural correlations with hexagonal symmetry and suggest a cylindrical structure. At 20 wt % concentration of Fe_2O_3-OH NPs, the multiple scattering peaks were more obvious and the primary peak sharpens, indicating a cylindrical morphology with significantly stronger domain segregation than those observed at lower NP loadings. Further increasing nanoparticle loading up to 30 wt % leads to a loss of the multiple higher orders of reflection (not shown here), suggesting an upper bound to particle loading for maintaining strong order in this particular system. This number is slightly less than other systems that have been reported recently.[33] The loading of the NPs in block copolymer (BCP) nanocomposites is affected by multiple factors, such as the composition of block copolymers, the interaction of nanoparticle surface with the BCP segments, and crystallinity, if present, in the BCP segments. In this work, the NPs were accommodated by the PAN phase in PAN (60)-*b*-PtBA (40) in which the target PAN domain is present at a weight fraction of 60%. Systems in which the target domain represents a larger fraction of the template will accommodate a higher overall loading of NPs, even at equivalent loadings within the target domains. Another limiting factor relates to the crystallization in the PAN segment. The crystallization of one block of a block copolymer can certainly influence both NP loading, by exclusion of NPs from crystallites, and microphase separation. In the current work, the morphology was characterized at room temperature after thermal annealing at 120 °C for 36 h, which is below the melting point of PAN (>300 °C) and higher than its degradation temperature. Therefore, in the following context, only 10 and 20 wt % loadings of Fe_2O_3-OH NPs will be discussed.

Comparison of the full width at half-maximum (FWHM) of the primary peaks of the SAXS profiles provides a comparison of the degree of order in BCP systems.[35,46] Smaller FWHM corresponds to a higher degree of segregation and overall order. Gaussian curve fitting results indicate that the FWHM value for blends with 20% Fe_2O_3-OH NPs (0.035 nm^{-1}) is significantly smaller than that of blends with 10% Fe_2O_3-OH NPs (0.052 nm^{-1}). The smaller FWHM corresponds to a higher degree of spatial correlation, which in turn indicates an increase in segregation strength and stronger order in the material upon addition of the functionalized nanoparticles. The narrowing of the scattering patterns because of increased segregation strength upon addition of the functionalized nanoparticles is consistent with the behavior of other systems that exhibit additive-driven assembly that we have recently reported.[33,34]

A closer look at the position of the primary peak shifting with increasing the loading of Fe_2O_3-OH NPs reveals some important features of the phase behavior of the composite. The primary scattering peak in Figure 2a shifts to larger *q*, indicative of a decrease in *d* spacing after incorporation of Fe_2O_3-OH nanoparticels. This is evidence that the nanoparticles selectively incorporate into the PAN domains and increase the segregation strength. If the nanoparticles were distributed into both domains and did not influence segregation strength, then shifting of the primary scattering peak to higher *q* would not occur.

Transmission electron microscopy (TEM) images in Figure 2b,c confirms this structural characterization. Figure 2b shows a TEM image of a microtomed sample of a blend with a 10 wt % concentration of Fe_2O_3-OH NPs. Periodic nanostructure was observed. Figure 2c shows that with 20 wt % of Fe_2O_3-OH

dx.doi.org/10.1021/cm404199z | *Chem. Mater.* 2014, 26, 2128−2137

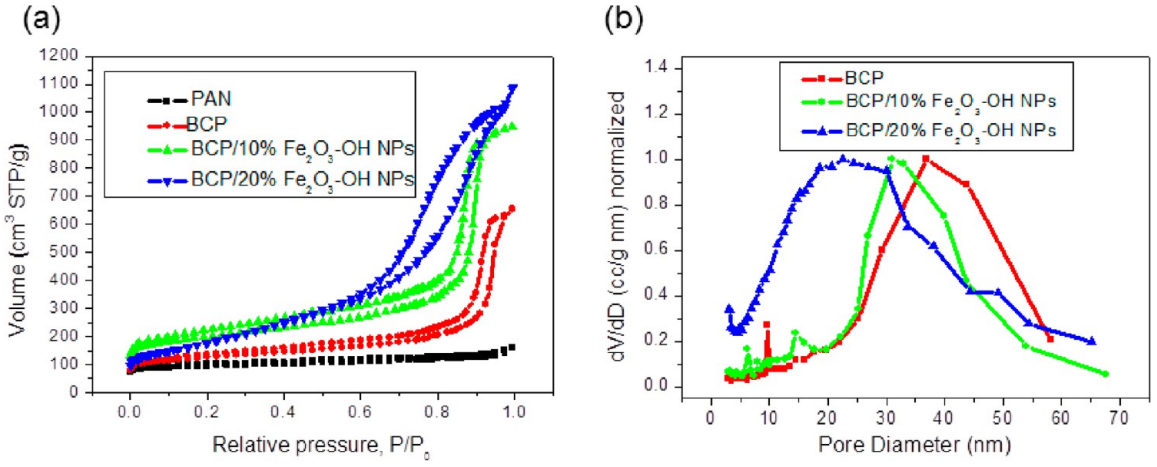

Figure 4. Pore-characterization results for various carbon materials: (a) nitrogen adsorption−desorption isotherms at 77 K and (b) the corresponding pore-size distribution curves calculated by the BJH method using adsorption braches of the isotherms.

Table 1. Data Summary from N_2 Sorption and Desorption Isotherms

	PAN	PtBA-*b*-PAN	10 wt % Fe_2O_3-OH	20 wt % Fe_2O_3-OH
S_{BET} (m^2/g)	301	414	540	757
pore diameter (nm)	n/a	31.9	26.0	21.0
total pore volume (cc/g)[a]	0.21	0.94	1.08	1.35

[a] V_{tot} calculated based on the amount adsorbed at a relative pressure of 0.97.

NPs, a well-ordered cylindrical morphology became evident. We note that PtBA and PAN have similar electron densities and thus the contrast observed by TEM in the absence of staining is another clear indication that Fe_2O_3-OH NPs selectively reside in the PAN domains.

Characterization of Mesoporous Carbon/Fe_2O_3-OH NPs Composites. Bulk and thin-film samples of the BCP/NP composites after thermal annealing were subjected to stabilization by 2 h annealing at 280 °C in contact with air and were subsequently pyrolyzed by heating at 10 °C/min to 700 °C under a nitrogen flow. Upon pyrolysis, the PAN (or PAN-nanoparticle) domains are converted into carbon (or carbon-nanoparticle composites), whereas the sacrificial porogen, PtBA, decomposes and is volatilized leaving the pores. The morphology and pore-size distribution of porous carbon materials obtained after pyrolysis were characterized with SAXS. Figure S3 shows small-angle X-ray scattering (SAXS) profiles for PtBA-*b*-PAN and blends of this BCP with Fe_2O_3-OH NPs at several NPs concentrations after carbonization. The nanocomposites exhibit two peaks even up to 20 wt % Fe_2O_3-OH NPs, indicating that the morphology induced from phase separation of block copolymer was retained. The FWHM values of the primary peaks are 0.125, 0.065, and 0.062 nm^{-1} for neat porous carbon with 10 wt % Fe_2O_3, and 20 wt % Fe_2O_3, respectively. These values are slightly higher than their analogues before carbonization, suggesting a lower degree of segregation and overall order. Nevertheless, comparing the composites with nanoparticles to the neat carbon materials, the FWHM value gradually decreases with the increase of nanoparticles loading, indicating that the incorporation of Fe_2O_3-OH nanoparticels improved the degree of order. This once again suggested that the nanoparticle-driven assembly approach is applicable to a wide range of nanoparticles and block copolymers and is a general approach to prepare well-ordered hybrid materials.

TEM was used to examine the mesostructure in more detail (Figure 3). As a control experiment, PAN homopolymer was also subjected to carbonization. Figure 3a shows the result from PAN homopolymer samples; although large defects are apparent, there is no evidence of a mesoporous structure. PtBA-*b*-PAN after pyrolysis is shown in Figure 3b, and the image reveals obvious mesostructure. Note that although there is not sufficient electron density contrast to reveal the morphology in the unpyrolyzed PtBA-*b*-PAN thin films, the removal of sacrificial PtBA domains through volatilization provided enough electron density contrast to see the morphology clearly. Although neat PtBA-*b*-PAN after pyrolysis showed a porous structure, the pores are not well-ordered. Micrographs of BCP/10% Fe_2O_3-OH NPs (Figure 3c) and BCP/20% Fe_2O_3-OH NPs (Figure 3d) films exhibit a uniform, nonfractal, nanoporous structure after pyrolysis. The degree of order is higher than that of neat BCP, which is consistent with the previously discussed SAXS results, and the characteristic length of the features is in good agreement with the position of the primary peak observed in SAXS patterns. The pore size decreased as the loading of Fe_2O_3-OH NPs increased. In addition to the mesopores, nanoparticles are also clearly visible in micrographs taken at higher magnification (Figure 3e). The nanoparticles are distributed throughout the wall framework; nanoparticle sizes are less than 4 nm, and no large aggregations of particles were observed.

Pore-size distribution and specific surface area play a vital role in mechanical, thermal, and chemical properties of the porous materials and their utility for electrodes. Direct information about the porosity of the samples was obtained through standard nitrogen adsorption analysis. The nitrogen adsorption−desorption isotherms are shown in Figure 4a. Except for the control PAN homopolymer sample, all the three isotherms are typical type-IV isotherms with an H_1-type hysteresis loop, representative of mesoporous structures. The corresponding pore-size distribution (PSD) curves, which were

dx.doi.org/10.1021/cm404199z | *Chem. Mater.* 2014, 26, 2128−2137

calculated from the adsorption branches of the isotherms using the Barrett–Joyner–Halenda (BJH) method, are shown in Figure 4b. The average pore diameter decreases from 31.9 to 26.0 to 21.0 nm when Fe_2O_3-OH NPs concentration increases in the original blend from 0 to 10 to 20 wt %, respectively. This decrease in the average pore size is consistent with the decreased *d* spacing determined from SAXS and the smaller pores observed by TEM and is expected to lead to larger specific surface areas and higher porosities. The Brunauer–Emmett–Teller (BET) specific surface area (S_{BET}) and the total pore volume per gram (V_{tot}) of the mesoporous samples calculated from nitrogen adsorption analysis are summarized in Table 1. S_{BET} and V_{tot} both increased with increasing nanoparticles loadings. It is remarkable that the S_{BET} value of the 20 wt % Fe_2O_3-OH nanoparticles sample was estimated to be 757 m^2/g, a relatively high value for the mesoporous carbon materials derived from polymer templates.[47] All of these results provide a strong indication that the overall nanoscale morphologies of block copolymer/nanoparticle composites were retained after decomposition of the sacrificial block and carbonization of the PAN blocks.

To confirm iron oxide incorporation into the carbon framework, X-ray photoelectron spectroscopy (XPS) was carried out. As shown in Figure 5 and Table 2, XPS analysis revealed a high iron content in composites, with 4.3 atom % in materials prepared using 10 wt % Fe_2O_3-OH NPs blend and 8.0 atom % in materials prepared using 20 wt % Fe_2O_3-OH NPs blends, indicating that after accounting for loss of the ligand shell the Fe_2O_3NP cores are incorporated into the carbon framework at very high yield. The mass loading of Fe_2O_3 in the final carbon composites therefore equals 16 wt % for materials derived from the 10 wt % Fe_2O_3-OH NPs blends and 30 wt % for the materials derived from the 20 wt % Fe_2O_3-OH NPs blends. Nitrogen is also abundant in the composites at concentrations as high as 13 atom %. It is worth noting that the N 1s peak in XPS in Figure 5 shows fine structure, consistent with the literature results for carbons derived from PAN.[45] The multiple model peaks correspond to nitrogen atoms in different chemical environments (i.e., pyridinic, pyrrolic, pyridine oxide, etc.). These nitrogen atoms have been demonstrated to be electrochemically active, which is in favor of our application.

Mesoporous Carbon/Fe_2O_3-OH NPs Composites As Electrode Materials for Supercapacitors. Ordered mesoporous materials generally exhibit high specific surface areas, which are attractive for supercapacitor applications. However, the energy-storage density in supercapacitors is still inferior in comparison with batteries. The incorporation of electrochemically active phases such as metal oxides is particularly promising to overcome this limitation because the introduction of an additional charge-storage mechanism (i.e., pseudocapacitance) involving fast and reversible redox reactions. The performance of mesoporous carbon/Fe_2O_3 thin films on stainless steel substrates as working electrodes was evaluated. No other additives such as carbon black or poly(vinylidene difluoride) (PVDF) binders were added. In this way, the experimental results reflected the electrochemical properties of only the active materials without conductive additives or binders. One molar aqueous Na_2SO_3 was chosen as the electrolyte. Other electrolytes such as KOH or Na_2SO_4 were also investigated, but the capacitances were lower than that of Na_2SO_3. This is consistent with literature results[48] wherein mechanistic studies indicate that in the case of Na_2SO_3 solution the capacitive

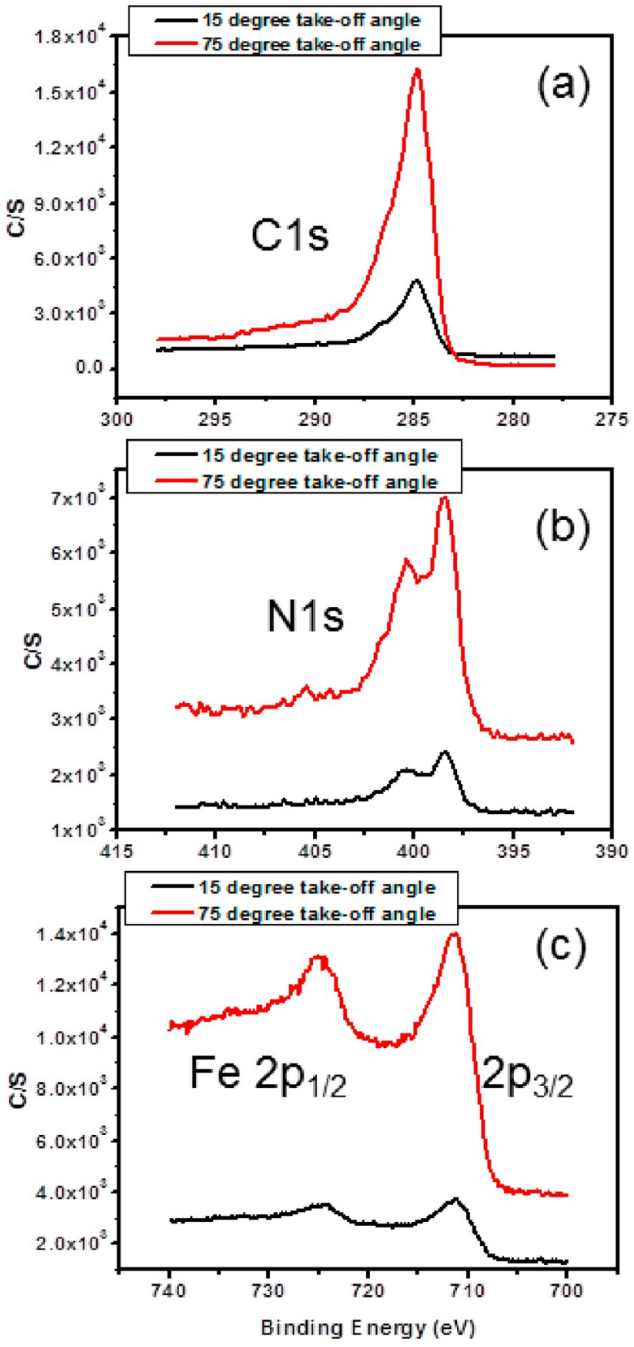

Figure 5. XPS results of PtBA-*b*-PAN/20% Fe_2O_3-OH nanoparticles (equal to 30 wt % Fe_2O_3 NPs after pyrolysis): (a) carbon 1s region, (b) nitrogen 1s region, and (c) iron 2p region.

current results from the combination of EDLC and pseudocapacitance that involves successive reduction of the specifically adsorbed sulfite anions. In Na_2SO_4(aq), the capacitive current is entirely due to EDLC. In the case of KOH(aq), the formation of an insulating layer by surface oxidation of the electrode results in a significantly lower capacitance.

The electrochemical measurements included cyclic voltammetry (CV), Figure 6a, galvanostatic charge/discharge (GCD), Figure 6b,c, and cycling stability, Figure 6d,e. The CV curve for neat mesoporous carbon electrodes derived from the BCP is relatively flat and rectangular, which is typical for electrochemical double-layer capacitors.[20,49] Even at a high scan rate of

dx.doi.org/10.1021/cm404199z | *Chem. Mater.* 2014, 26, 2128–2137

Table 2. XPS Data Summary

	C (atom %)		N (atom %)		O (atom %)		Fe (atom %)	
takeoff angle	15°	75°	15°	75°	15°	75°	15°	75°
PtBA-*b*-PAN	78.9	78.7	15.0	15.4	6.1	5.9	0.0	0.0
10 wt % Fe_2O_3-OH NPs	71.3	70.4	12.9	13.8	1.6	11.3	4.2	4.5
20 wt % Fe_2O_3-OH NPs	65.1	65.0	11.7	12.4	15.4	14.3	7.8	8.3

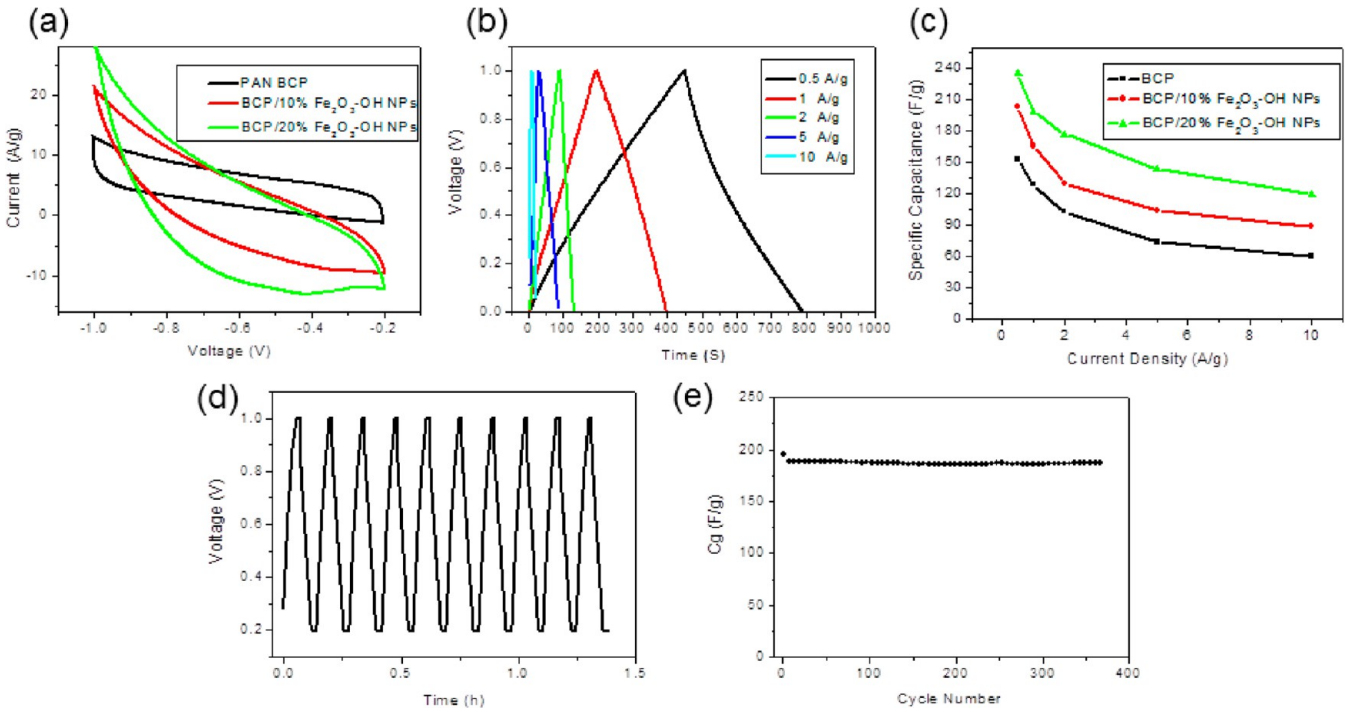

Figure 6. Characterization of supercapacitors built with mesoporous carbon electrodes: (a) cyclic voltammetry curves at a scanning rate of 100 mV/s, (b) galvanostatic charge−discharge curves, (c) relationship between specific capacitance and current density for various of electrodes, and (d, e) cycling performance at 1 A/g. All measurements were recorded in 1 M Na_2SO_3 aqueous electrolyte with a Pt wire counter electrode and a Ag/AgCl reference electrode.

100 mV/s, the CV curve showed rectangular shape, implying fast electrolyte movement. The addition of the Fe_2O_3 NPs increased the integrated area of the CV curves, suggesting increased specific capacitance of the films. Importantly, the CV curves became less rectangular, and a shallow redox reaction hump at −0.42 V versus Ag/AgCl was also present. This originates from the pseudocapacitance of the Fe_2O_3 NPs. It had been suggested that the mechanism for the pseudocapacitance behavior of Fe_2O_3 is similar to that proposed for Fe_3O_4.[50] According to the work of Wu et al.,[51] the pseudocapacitance reaction mechanisms of magnetite in Na_2SO_3 may result from the surface redox reaction of sulfur in the form of sulfate and sulfite anions as well as the redox reactions between Fe^{II} and Fe^{III} accompanied by intercalation of sulfite ions to balance the extra charge associated with the iron oxide layers. These mechanisms are tentative and have yet to be verified.

The discharge behavior of the electrode was examined by a galvanostatic charge/discharge (GCD) test in the potential range from −1.0 to 0.1 V at different current densities. We calculated the capacitance of the films as $C = I/(dV/dt)$, where C is capacitance, I is the current, and V is the potential.[52] For the pure mesoporous carbon film, the specific capacitance (C_g) was found to be 153 F/g at a current density of 0.5 A/g. This capacitance agrees well with the capacitance for a mesoporous carbon powder from a PAN BCP template.[45] The typical capacitance of mesoporous carbon without any heteroatoms is usually less than 100 F/g, although there is a report of a 112 F/g capacitance of a carbon from CV measurement at a low scan rate of 5 mV/s.[49] Herein, the nitrogen atoms preserved from PAN contribute to the electrochemical reaction and lead to higher specific capacitance. The addition of 10 wt % Fe_2O_3 NPs (equal to 16 wt % Fe_2O_3 NPs after pyrolysis) significantly increases the capacitance to 204 F/g at a current density of 0.5 A/g, and the addition of 20 wt % Fe_2O_3 NPs (equals to 30 wt % Fe_2O_3 NPs after pyrolysis) increases it 235 F/g at a current density of 0.5 A/g, which is 54% larger than that of pristine mesoporous carbon. This enhanced capacitance is consistent with the ease of accessibility of the iron oxide in the mesoporous carbon framework. Previous reports indicate that iron oxide/activated carbon composites yield specific capacitance up to 188 F/g.[53] Improvements in the specific capacitance realized in this study may be due to both the excellent dispersion of small nanoparticles and the orderd mesoporous carbon structure. In addition, an iron oxides/reduced graphene oxide composite with a high capacitance of 326 F/g at 0.5 A/g was achieved because of the extraordinarily large surface area and high electrical conductivity of graphene.[54] However, graphene carries other drawbacks including high cost and limited processablilty.

dx.doi.org/10.1021/cm404199z | *Chem. Mater.* 2014, 26, 2128−2137

We also studied GCD at different loading current density ranges from 0.5 to 10 A/g. Figure 6b showed the GCD curves for 20 wt % Fe_2O_3 NPs samples at different current densities. The constant slope of these discharge curves reveals good electrochemical reversibility and capacitive characteristics. The specific capacitance for the 20 wt % Fe_2O_3 NPs was found to be 235 F/g at a current density of 0.5 A/g, and it retained 51% of this value (119 F/g) at a high loading current density of 10 A/g, as seen in Figure 6c. This rate capability indicates that the interconnected mesoporous structure provides an efficient pathway for electrolyte ion movement through the carbon matrix.[55] The energy density (E) was calculated from the charge−discharge curves at different current densities according to the equation $E = 1/2C_g\Delta U^2$, where ΔU is the voltage difference. The energy density for the 20 wt % Fe_2O_3 NPs was 39.4 W h/kg at a current density of 0.5 A/g and 20.0 W h/kg at a current density of 10 A/g. In addition to the initial capacitance of the materials, the cyclic performance is critical for supercapacitor applications. Importantly, the devices derived from the 20 wt % Fe_2O_3 NPs samples exhibit good cyclability by maintaining 95% of their capacitance after 380 charge/discharge cycles at 1 A/g, as shown in Figure 6d,e.

CONCLUSIONS

We report the development of ordered mesoporous carbon/iron oxide composites by cooperative self-assembly of PtBA-*b*-PAN block copolymers that contain both a carbon precursor and a porogen and phenol-functionalized iron oxide nanoparticles followed by carbonization. The strong interactions between phenol-functionalized iron oxide nanoparticles and polyacrylonitrile result in a preferential dispersion of the nanoparticles within the PAN domains and leads to an ordered nanostructured mesoporous carbon framework containing as high as 30 wt % iron oxide nanoparticles after pyrolysis. The resulting iron oxide NPs/mesoporous carbon composites exhibit high specific surface areas (540−757 m^2/g) and high pore volumes (1.08−1.35 cm^3/g). The specific capacitance of neat mesopororous carbon films prepared from PtBA-*b*-PAN was 153 F/g at a current density of 0.5 A/g, whereas films containing 16 and 30 wt % Fe_2O_3 NPs exhibited capacitances of 204 and 235 F/g, respectively. Moreover, 95% of the initial capacitance was maintained after more than 380 cycles for the composites. This work demonstrates a simple and easily scaled approach to prepare ordered mesoporous carbon composites that possess attractive electrochemical properties for energy-storage applications.

ASSOCIATED CONTENT

Supporting Information

Synthetic scheme of PtBA-*b*-PAN block copolymer; FTIR spectra of PtBA-*b*-PAN, Fe_2O_3-OH nanoparticles, and their blend; and overlay of SAXS profiles of block copolymer and its blends with Fe_2O_3-OH nanoparticles after carbonization (PDF). This material is available free of charge via the Internet at http://pubs.acs.org.

AUTHOR INFORMATION

Corresponding Author

*E-mail: watkins@polysci.umass.edu.

Notes

The authors declare no competing financial interest.

ACKNOWLEDGMENTS

Funding from the NSF Center for Hierarchical Manufacturing (CMMI-1025020) is gratefully acknowledged.

REFERENCES

(1) Simon, P.; Gogotsi, Y. *Nat. Mater.* **2008**, *7*, 845.
(2) Pandolfo, A. G.; Hollenkamp, A. F. *J. Power Sources* **2006**, *157*, 11.
(3) Wang, H.; Li, Z.; Yang, J.; Li, Q.; Zhong, X. *J. Power Sources* **2009**, *194*, 1218.
(4) Liang, C.; Li, Z.; Dai, S. *Angew. Chem., Int. Ed.* **2008**, *47*, 3696.
(5) Wang, Y.; Shi, Z.; Huang, Y.; Ma, Y.; Wang, C.; Chen, M.; Chen, Y. *J. Phys. Chem. C* **2009**, *113*, 13103.
(6) Futaba, D. N.; Hata, K.; Yamada, T.; Hiraoka, T.; Hayamizu, Y.; Kakudate, Y.; Tanaike, O.; Hatori, H.; Yumura, M.; Iijima, S. *Nat. Mater.* **2006**, *5*, 987.
(7) Frackowiak, E.; Beguin, F. *Carbon* **2002**, *40*, 1775.
(8) Zhai, Y.; Dou, Y.; Zhao, D.; Fulvio, P. F.; Mayes, R. T.; Dai, S. *Adv. Mater.* **2011**, *23*, 4828.
(9) Zhang, L. L.; Zhao, X. S. *Chem. Soc. Rev.* **2009**, *38*, 2520.
(10) Toupin, M.; Brousse, T.; Bélanger, D. *Chem. Mater.* **2002**, *14*, 3946.
(11) Lao, Z. J.; Konstantinov, K.; Tournaire, Y.; Ng, S. H.; Wang, G. X.; Liu, H. K. *J. Power Sources* **2006**, *162*, 1451.
(12) Yu, Z.; Duong, B.; Abbitt, D.; Thomas, J. *Adv. Mater.* **2013**, *25*, 3302.
(13) Zhao, X. Z. X.; Sanchez, B. M.; Dobson, P. J.; Grant, P. S. *Nanoscale* **2011**, *3*, 839.
(14) Xia, H.; Lai, M. O.; Lu, L. *JOM* **2011**, *63*, 54.
(15) Laforgue, A.; Simon, P.; Sarrazin, C.; Fauvarque, J.-F. *J. Power Sources* **1999**, *80*, 142.
(16) Rudge, A.; Davey, J.; Raistrick, I.; Gottesfeld, S.; Ferraris, J. P. *J. Power Sources* **1994**, *47*, 89.
(17) Mastragostino, M.; Arbizzani, C.; Soavi, F. *J. Power Sources* **2001**, *97−98*, 812.
(18) Snook, G. A.; Kao, P.; Best, A. S. *J. Power Sources* **2011**, *196*, 1.
(19) Jiang, H.; Ma, J.; Li, C. Z. *Adv. Mater.* **2012**, *24*, 4197.
(20) Dai, M.; Song, L.; LaBelle, J. T.; Vogt, B. D. *Chem. Mater.* **2011**, *23*, 2869.
(21) Fischer, A. E.; Saunders, M. P.; Pettigrew, K. A.; Rolison, D. R.; Long, J. W. *J. Electrochem. Soc.* **2008**, *155*, A246.
(22) Nagao, M.; Otani, M.; Tomita, H.; Kanzaki, S.; Yamada, A.; Kanno, R. *J. Power Sources* **2011**, *196*, 4741.
(23) Yang, C. M.; Sheu, H. S.; Chao, K. J. *Adv. Funct. Mater.* **2002**, *12*, 143.
(24) Huwe, H.; Fröba, M. *Microporous Mesoporous Mater.* **2003**, *60*, 151.
(25) Gu, Z.; Deng, B.; Yang, J. *Microporous Mesoporous Mater.* **2007**, *102*, 265.
(26) Dong, X.; Shen, W.; Gu, J.; Xiong, L.; Zhu, Y.; Li, H.; Shi, J. *J. Phys. Chem. B* **2006**, *110*, 6015.
(27) Zhu, S.; Zhou, H.; Hibino, M.; Honma, I.; Ichihara, M. *Adv. Funct. Mater.* **2005**, *15*, 381.
(28) Liu, R.; Shi, Y.; Wan, Y.; Meng, Y.; Zhang, F.; Gu, D.; Chen, Z.; Tu, B.; Zhao, D. *J. Am. Chem. Soc.* **2006**, *128*, 11652.
(29) She, L.; Li, J.; Wan, Y.; Yao, X.; Tu, B.; Zhao, D. *J. Mater. Chem.* **2011**, *21*, 795.
(30) Zhai, Y.; Dou, Y.; Liu, X.; Tu, B.; Zhao, D. *J. Mater. Chem.* **2009**, *19*, 3292.
(31) Li, J.; Gu, J.; Li, H.; Liang, Y.; Hao, Y.; Sun, X.; Wang, L. *Microporous Mesoporous Mater.* **2010**, *128*, 144.
(32) Baumann, T. F.; Fox, G. A.; Satcher, J. H.; Yoshizawa, N.; Fu, R.; Dresselhaus, M. S. *Langmuir* **2002**, *18*, 7073.
(33) Lin, Y.; Daga, V. K.; Anderson, E. R.; Gido, S. P.; Watkins, J. J. *J. Am. Chem. Soc.* **2011**, *133*, 6513.
(34) Wei, Q.; Lin, Y.; Anderson, E. R.; Briseno, A. L.; Gido, S. P.; Watkins, J. J. *Acs Nano* **2012**, *6*, 1188.

(35) Lin, Y.; Lim, J. A.; Wei, Q.; Mannsfeld, S. C. B.; Briseno, A. L.; Watkins, J. J. *Chem. Mater.* **2012**, *24*, 622.
(36) Kowalewski, T.; Tsarevsky, N. V.; Matyjaszewski, K. *J. Am. Chem. Soc.* **2002**, *124*, 10632.
(37) Park, J.; Kang, E.; Son, S. U.; Park, H. M.; Lee, M. K.; Kim, J.; Kim, K. W.; Noh, H. J.; Park, J. H.; Bae, C. J.; Park, J. G.; Hyeon, T. *Adv. Mater.* **2005**, *17*, 429.
(38) Wang, X.; Tilley, R. D.; Watkins, J. J. *Langmuir* **2014**, *30*, 1514.
(39) Jain, M.; Abhiraman, A. S. *J. Mater. Sci.* **1987**, *22*, 278.
(40) Leiston-Belanger, J. M.; Penelle, J.; Russell, T. P. *Macromolecules* **2006**, *39*, 1766.
(41) Le Questel, J.-Y.; Berthelot, M.; Laurence, C. *J. Phys. Org. Chem.* **2000**, *13*, 347.
(42) Wang, Z.; Huang, B.; Huang, H.; Chen, L.; Xue, R.; Wang, F. *Electrochim. Acta* **1996**, *41*, 1443.
(43) Leibler, L. *Macromolecules* **1980**, *13*, 1602.
(44) Zhang, F.; Stühn, B. *Colloid Polym. Sci.* **2006**, *284*, 823.
(45) Zhong, M.; Kim, E. K.; McGann, J. P.; Chun, S.-E.; Whitacre, J. F.; Jaroniec, M.; Matyjaszewski, K.; Kowalewski, T. *J. Am. Chem. Soc.* **2012**, *134*, 14846.
(46) Tirumala, V. R.; Romang, A.; Agarwal, S.; Lin, E. K.; Watkins, J. J. *Adv. Mater.* **2008**, *20*, 1603.
(47) Meng, Y.; Gu, D.; Zhang, F.; Shi, Y.; Cheng, L.; Feng, D.; Wu, Z.; Chen, Z.; Wan, Y.; Stein, A.; Zhao, D. *Chem. Mater.* **2006**, *18*, 4447.
(48) Wang, S.-Y.; Ho, K.-C.; Kuo, S.-L.; Wu, N.-L. *J. Electrochem. Soc.* **2006**, *153*, A75.
(49) Li, H.-Q.; Liu, R.-L.; Zhao, D.-Y.; Xia, Y.-Y. *Carbon* **2007**, *45*, 2628.
(50) Nagarajan, N.; Zhitomirsky, I. *J. Appl. Electrochem.* **2006**, *36*, 1399.
(51) Wu, N.-L.; Wang, S.-Y.; Han, C.-Y.; Wu, D.-S.; Shiue, L.-R. *J. Power Sources* **2003**, *113*, 173.
(52) Wang, J.; Polleux, J.; Lim, J.; Dunn, B. *J. Phys. Chem. C* **2007**, *111*, 14925.
(53) Luo, P. W.; Yu, J. G.; Shi, Z. Q.; Huang, H.; Liu, L.; Zhao, Y. N.; Li, G. D.; Zou, Y. C. *Chem. Res. Chin. Univ.* **2012**, *28*, 780.
(54) Qu, Q.; Yang, S.; Feng, X. *Adv. Mater.* **2011**, *23*, 5574.
(55) Liang, Y.; Wu, D.; Fu, R. *Langmuir* **2009**, *25*, 7783.